

CALIFORNIA STATE UNIVERSITY, NORTHRIDGE

Multifractal Properties of Intensity Signals in Solar Coronal Holes, Adjacent Quiet Sun, and  
Boundary Regions in the Context of the Magnetic Network

A thesis submitted in partial fulfillment of the  
requirements for the degree of Master of Science in Physics

By  
Landon Wells

August 2022

Copyright by Landon Wells 2022

The thesis of Landon Wells is approved :

---

Dr. Damian Christian

---

Date

---

Dr. Debi Prasad Choudhary

---

Date

---

Dr. Ana Cristina Cadavid, Chair

---

Date

CALIFORNIA STATE UNIVERSITY, NORTHRIDGE

## Table of Contents

Copyright	ii
Signature Page	iii
List of Figures	vi
List of Tables	viii
Abstract	ix
1. Introduction	1
2. Mathematical Background and Analysis Methods	5
2.1 The Hurst Exponent, Stationary and Non-Stationary Processes	5
2.2 Detrended Fluctuation Analysis	7
2.3 Multifractal Detrended Fluctuation Analysis	9
2.4 The Effect of Noise	11
2.5 Potential Magnetic Field Extrapolation	13
2.6 k-means Clustering	13
3. Data and Data Preparation	15
3.1 Description of the Data	15
3.2 Defining a Coronal Hole Boundary, CHARM and CHIMERA	17
3.3 Defining Magnetic Field Boundaries	18
4. Results	19
4.1 Analysis Strategy and Case Selection	19

4.2 Exploration of the Data Set	20
5. Summary and Discussion of Results	24
5.1 3-Dimensional Parameter Space: Initial Classification	24
5.2 3-Dimensional Parameter Space: k-means Clustering	26
5.3 Reshuffled Time Series and Upsurges	29
6. Conclusions and General Outlook	32
Bibliography	34

## List of Figures

1	Cartoon showing the sequence of steps in an interchange reconnection event. a) Open field lines and a closed loop approach each other. b) An open field line reconnects with a closed field line. The topology changes leading to a reconfigured open field line with an S-shape structure and a new small closed loop. c) The S-shape structure (switchback) and plasma propagates outward. Adapted from Zank et. al. (2020) (6).	1
2	An artist's rendition of the solar atmosphere, Böhm et. al. (2008). (23).	3
3	Examples of common time-series observed in nature. The data is obtained from the AIA 193 A data used in the analysis. The Y-axis is in arbitrary units and the X-axis is in units of image number.	5
4	Fluctuation function vs scale and generalized Hurst exponent vs moment for artificial data. Left panels: monofractal. Right panels: multifractal.	10
5	Fluctuation functions $F_q(s)$ (left) and generalized Hurst exponents $h(q)$ (right) for multifractal time series with added white noise of zero mean, unit variance, and amplitude $A$ . The scaling exponents are calculated for the large scale range $10^3 < s < 10^4$ . $A = 0$ (a) and (b). $A = 0.1$ (c) and (d). $A = 1.0$ (e) and (f). $A = 10$ (g) and (h). From Ludescher et. al. (2011) (53).	12
6	Three figures depicting the data before, and after analysis. (a) AIA 193A image of the CH used in the creation of the CHIMERA boundary. Fifteen boxes within the figure define the regions used for the MF-DFA analysis. (b) Contemporaneous LOS HMI image used in the creation of the magnetic field boundaries. (c) Unscaled $\alpha$ map created via the DFA.	16
7	The above image exemplifies the process of selecting a case. The image is of the unscaled $\alpha$ values obtained over each pixel in the sub-region. The boundaries of the CHARM, CHIMERA, and magnetic network are seen overlaid. Pixels are shown being selected with which the average multifractal spectrum is calculated across.	19
8	Three sets of figures depicting an example of a monofractal, (a) and (b), multifractal with noise, (c) and (d), and a multifractal, (e) and (f), obtained from the data set.	21
9	Four figures showing the effect of the reshuffling process. (Left) The original time series. (Right) The reshuffled time series. The top series remains multifractal after reshuffling due to intermittency in the time series.	22
10	Summary of results for the 190 cases. Top-left: the three parameter space. Top-right: projection onto the $\Delta H - H_{sp}$ plane. Bottom-left: projection onto the $\zeta$ vs $\alpha$ plane. Bottom-right: projection onto the $\zeta$ vs $\Delta H - H_{sp}$ plane.	25
11	Summary of results for the 190 cases after the K-means clustering algorithm is performed. Top-left: the clusters in three parameter space. Top-right: projection onto the $\Delta H - H_{sp}$ plane. Bottom-left: projection onto the $\zeta$ vs $\alpha$ plane. Bottom-right: projection onto the $\zeta$ vs $\Delta H - H_{sp}$ plane.	27
12	Figure (a) depicts the flux imbalance ratio versus the reshuffled reduced multifractality. Figure (b) shows the not shuffled fluctuations of the case which had the largest degree of multifractality after reshuffling.	29

- 13 Image displaying an example of a large spiking event in which the MF-DFA method failed to determine the long-range correlations of the time series due to intermittency. The pixels gathered are from a long lasting solar storm in the coronal hole that had ended at the beginning of the time series. 30
- 14 Example of a potential field line of sight extrapolation. The figure shows some open loops ejecting from the center of the region followed by small closed loops along the outer edge of the extrapolated region, indicating the presence of a magnetic reconnection, or interchange re-connection, based event. 31

## List of Tables

1	Table depicting the number of cases from each region in each quadrant for the respective graphs.	25
2	Summary of results classified according to the number of elements in a cluster in a given region.	28
3	Summary of results classified according to the number of cases in a region in a given cluster.	28



## Abstract

# Multifractal Properties of Intensity Signals in Solar Coronal Holes, Adjacent Quiet Sun, and Boundary Regions in the Context of the Magnetic Network

By

Landon Wells

Master of Science in Physics

Coronal holes are regions in the Sun characterized by a predominance of open magnetic fields, as well as lower densities and temperatures than their surrounding regions. There is interest in studying the properties of coronal holes because of their possible connection to the origin of the solar wind. Cadavid et. al. (2019) (1) used the method of detrended fluctuation analysis to investigate the scaling properties of EUV intensity fluctuations of three low latitude coronal holes (CH) and adjacent quiet-Sun (QS) regions, finding that the signals obeyed a scaling symmetry for a temporal range between  $\sim 20$  and  $\sim 60$  minutes, which indicated their fractal nature. The generalized Hurst exponents indicated that CH signals are primarily stationary and persistent, and surrounding QS signals are non-stationary and anti-persistent. This follow up study aims to investigate whether the CH and QS intensity signals are monofractal or multifractal requiring a multiplicity of scaling exponents to be described. Using EUV emission data obtained with the AIA instrument onboard the SDO satellite, the multifractality of the intensity fluctuations in an equatorial CH and adjacent QS is investigated using the method of multifractal detrended fluctuation analysis (MF-DFA). Contemporaneous magnetic images obtained with the SDO/HMI instrument provides physical context. Two methods were used to define the CH boundaries. The CH, QS, and “in-between” boundary regions all present cases of monofractality, noisy multifractality, and multifractality, the latter primarily due to long range correlations. Results are classified into 4 clusters in a 3-dimensional parameter space. The CH network tends to primarily include (persistent, multifractal) signals. In the QS and in-between regions this tendency is present but lower. Away from the network all regions tend to have comparable percentages of (persistent, multifractal) and (anti-persistent, not multifractal) cases. The network multifractality appears in regions of possible interchange reconnection, a process shown to be related to the mechanism of energy transfer to the solar wind.

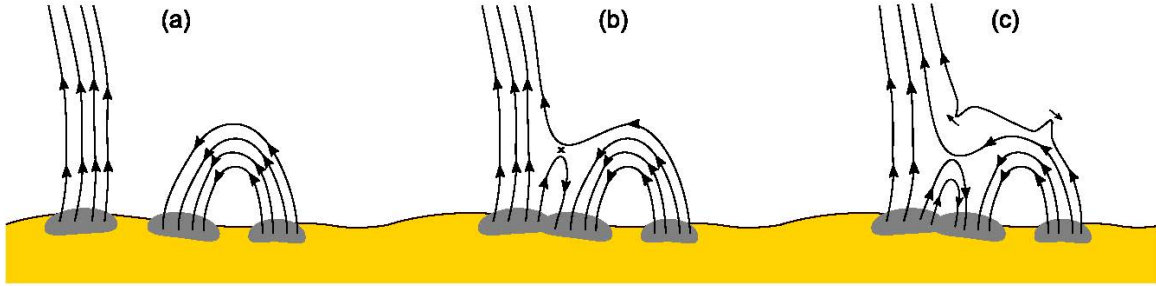


Figure 1: Cartoon showing the sequence of steps in an interchange reconnection event. a) Open field lines and a closed loop approach each other. b) An open field line reconnects with a closed field line. The topology changes leading to a reconfigured open field line with an S-shape structure and a new small closed loop. c) The S-shape structure (switchback) and plasma propagates outward. Adapted from Zank et. al. (2020) (6).

## 1. Introduction

Coronal holes (CH)s are regions in the solar corona characterized by open magnetic fields. Because the open field lines allow the plasma to escape into space, CHs have lower density and temperature than their surroundings and therefore appear as dark regions in extreme ultraviolet (EUV) and X-ray coronal emission (e.g. Cranmer (2009) (2), and references therein). Polar CHs, which tend to be more persistent, are the primary sources of the high speed ( $> \sim 500$  km/s) steadier solar wind. Furthermore it has been established that the high-speed stream peak velocity at Earth is related to the area of the CHs on the Sun (Krieger et. al. (1973) (3)). The origin of the slow ( $< \sim 500$  km/s), more spatially and temporally intermittent, solar wind is still a subject of debate. Possible sources include streamers, loops in quiet-Sun (QS) and active regions, and lower latitude CH boundaries (e.g. Abbo et. al. (2016) (4), Cranmer et. al. (2017) (5)).

In general, the fast solar wind has a plasma composition similar to that of the photosphere, while the composition of the slow solar wind is similar to that of coronal loops (Zurbuchen et. al. (2002) (7)). It has been suggested that by interchange reconnection between closed and open field lines, an example of which can be seen in Figure 1, which allows for the release of the closed coronal loop plasma, is a primary mechanism for the origin of the slow solar wind (Antiochos et. al. (2011) (8), Zank et. al. 2020 (6)). The dynamics underlying interchange reconnection at different spatial and temporal scales is driven by the turbulent photospheric motions (Higginson et. al. (2017) (9)). Figure 2 provides an illustration of the complexity of the solar atmosphere. At

supergranular scales (temporal scale of  $\sim 1$  day) the bipole structures are advected to the boundary of supergranular network cells where they reconnect with the open fields. In CH open flux funnels, the energy is released to accelerate outflows, while in regions with overlying closed loops (as in the QS), the energy is released into the loop structures (Tu et. al. (2005) (10); McIntosh et. al. (2007) (11); He et. al. (2010) (12)). This mechanism also is expected to allow for the boundaries to evolve so that the CHs can maintain their apparent rigid rotation (Sheeley et. al. (1987) (13); Madjarska & Wiegmann (2009) (14); Yang et. al. (2011) (15); Tian et. al. (2011) (16)), and can lead to the formation of jets, spicules and plumes (eg. Subramanian et. al. (2010) (17), Pariat et. al. (2015) (18)). At the smaller scales of granular flows and the magnetic carpet (Schrijver et. al. (1997) (19)), with temporal scales in the order of minutes, the energy released from interchange reconnection is expected to produce Alfvén wave “noise” which can heat the coronal plasma and drive the solar wind but not lead to the release of the closed-field plasma into the solar wind (Higginson et. al. (2017) (9)).

Observations by the Parker Solar Probe (PSP, Fox et. al. (2016) (20)), presented evidence of the slow solar wind originating in an equatorial coronal hole. The magnetic measurements showed sections of intermittent reversals “interspersed in a smoother and less turbulent flow with a near-radial magnetic field” (Bale et. al. (2019) (21)). Dudok de Wit et. al. (2020) (22) found that there was no typical range of deflections that defined a switchback. They did find that there were two slow solar wind states. One is characterized by turbulent fluctuations, small magnetic field deflections and “short memory.” In this scenario, photospheric motions drive the fluctuations which release energy in the corona via turbulent dissipation. The other state is characterized by larger deflections which tend to have a “longer memory.” Zank et. al. (2020) (6) proposed that these switchbacks characterized multiple large-amplitude radial magnetic field and velocity fluctuations, that each exhibit large and rapid magnetic field rotations, could be explained through interchange reconnection between large coronal loops ( $\sim 6R_{Sun}$ ) and open fields.

Because of their role as sources of the solar wind, CHs continue to be an active subject of research. For example, recent work by Reiss et. al. (2021) (24) investigated the high sensitivity of the physical CH properties such as the area, mean intensity, and mean magnetic field strength to

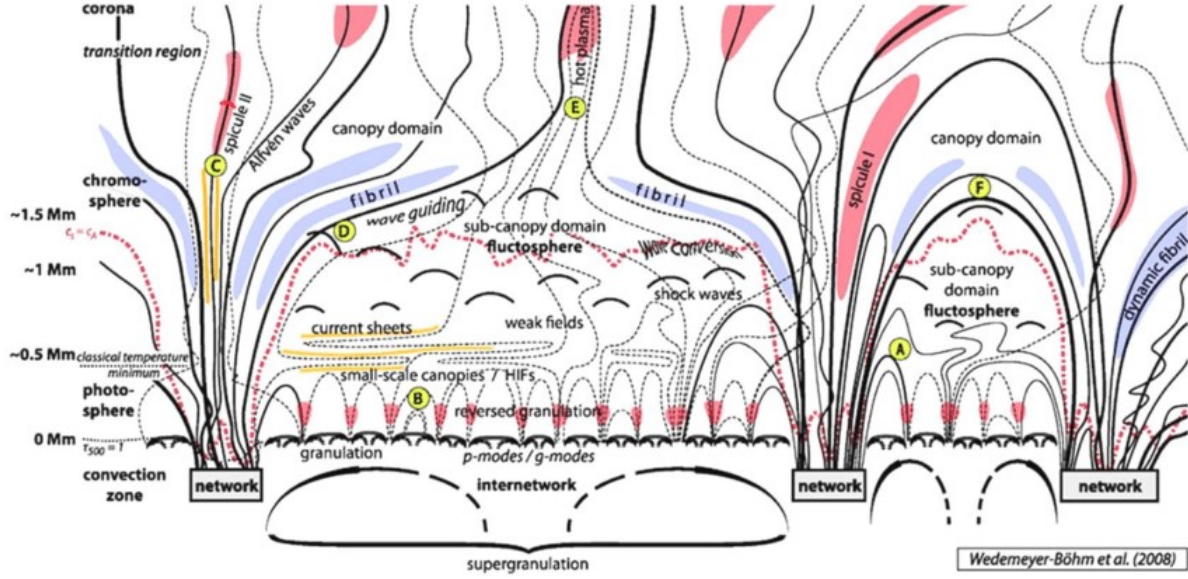


Figure 2: An artist's rendition of the solar atmosphere, Böhm et. al. (2008). (23).

the method of detection and boundary definition. While observations do not have access to the reconnection and energy release spatial scales, analysis of the cooling plasma intensity signals can provide information about the underlying heating processes (Klimchuk et. al. (2015) (25)). Using data from the Atmospheric Imaging Assembly (AIA) and the Helioseismic and Magnetic Imager (HMI) instruments on board the Solar Dynamics Observatory (SDO), Cadavid et. al. (2019) (26) investigated the dynamics of the stochastic component in the EUV emission of three low-latitude CHs and neighboring QS regions, by analyzing the scaling properties of the time series in the context of the magnetic field topology. They applied the method of detrended fluctuation analysis (DFA) which is used to identify the scaling properties and long-term correlations in stochastic time series after accounting for external trends (i.e., Peng et. al. (1994) (27); Chen et. al. (2002) (28); Hu et. al. (2001) (29); Kantelhardt et. al. (2002) (30)). By generating maps of a generalized Hurst exponent,  $\alpha$ , they found that in the QS regions and in CH sub-regions with magnetic bipoles, the scaling exponent corresponded to anti-correlated turbulent-like processes ( $1.0 < \alpha \leq 1.5$ ). In CHs and QS sub-regions associated with open magnetic fields the generalized exponent indicated positively-correlated (persistent) processes ( $0.5 < \alpha < 1$ ). In the latter case, the sub-regions occurred near the CH boundaries and were characterized by a higher flux imbalance ratio. To further

characterize the dynamics of the EUV emission, the present project investigates whether the intensity time signals are monofractal in the sense that their scaling properties can be fully described with the exponent  $\alpha$ , or if they are multi-fractal, and as such, require multiple scaling exponents. For this purpose the method of multifractal detrended fluctuation analysis (MF-DFA, Kantelhardt et. al. (2002) (30)) is used to analyze the scaling properties of a range of moments of the intensity time series of EUV emission in one CH and adjacent QS region located near disk center. Since DFA considers only the second moment of a time series, the scaling ranges used to identify the generalized Hurst exponent tend to be well defined for a single pixel time signal. For larger and for negative moments, an average must be taken over a collection of pixels. To take into account the ambiguity in the definition of the boundary of the CH, two methods have been applied leading to a partition of the data into three sets: inside the CH, in between the two boundaries, and outside the outer boundary which corresponds to the QS region.

Aiming to capture the full information from these three regions, MF-DFA has been applied to 190 subregions of about 100 pixels each. The information provided by MF-DFA in terms of the generalized Hurst exponent and the degree of multifractality is complemented by the calculation of the flux imbalance ratio that is shown to be a good proxy to separate network from not network regions. To gain insight into the results a k-means clustering algorithm was used to identify four clusters among the 190 cases in the three dimensional parameter space. There permitted the classification of the data into the groups (network, persistent, multifractal), (not network, persistent, multifractal), (network, anti-persistent, not multifractal), (not network, anti-persistent, not multifractal).

The thesis is organized as follows. Section 2 introduces the necessary the mathematical background and analysis methods. Section 3 describes the data and the data preparation including the techniques used to identify CH boundary. Section 4 reports on the results and Section 5, summarizes and discusses the results, as well as implications of the findings as they relate to the underlying mechanisms for energy release.

## 2. Mathematical Background and Analysis Methods

### 2.1 The Hurst Exponent, Stationary and Non-Stationary Processes

Spectra obeying a power law are encountered in a variety of astrophysical systems (Aschwanden 2011, and references therein). Recent examples for observations in the solar atmosphere include results for coronal emission (e.g. Auchère et. al. (2014) (31); Gupta et. al. (2014) (32); Cadavid et. al. (2014) (33); Ireland et. al. (2015) (34)) and chromospheric signals (e.g. Reardon et. al. (2008) (35); Lawrence et. al. (2011) (36); Krishna Prasad et. al. (2017) (37)). The motivation to use DFA in this study is based on two points: first, the fact that the time series of EUV coronal emission are nonstationary, and second, to have a technique which can quantify more precisely the scaling properties of individual pixel time series. Furthermore it is possible to relate the generalized Hurst exponent,  $\alpha$ , obtained with DFA, the original Hurst exponent,  $H$ , and the spectral power exponent,  $\beta$ , allowing us to make contact with standard results.

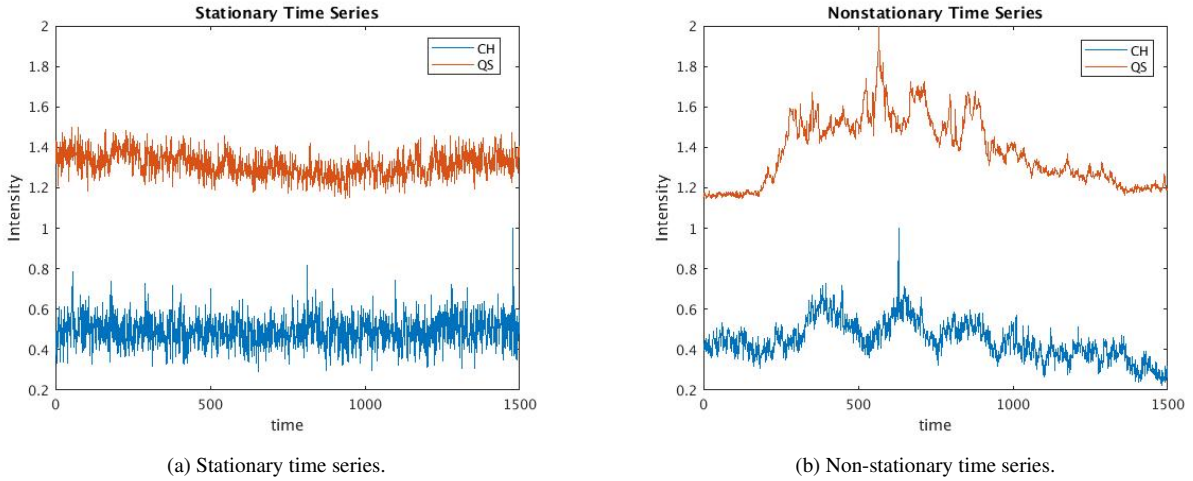


Figure 3: Examples of common time-series observed in nature. The data is obtained from the AIA 193 A data used in the analysis. The Y-axis is in arbitrary units and the X-axis is in units of image number.

As it is well known, the presence of a power law in the spectra is representative of an underlying scaling symmetry. In particular, self-similarity describes the property in which a part of a physical structure replicates the whole structure upon rescaling. In this case it is said that the structure is a fractal (e.g. Feder (1988) (38), and references therein). In the case of a time series in which the rescaling symmetry only applies to the time dimension and not to the amplitude of the signal, the

self-similarity (fractality) instead can be referred to as self-affinity Hardstone et. al. (2012) (39), which can be described in terms of the statistical properties of the time series.

A stochastic nonstationary process  $X(t)$  is self-affine (fractal) if it satisfies

$$X(\lambda t) \equiv \lambda^H X(t), \quad (1)$$

where  $\lambda$  is a scaling factor,  $0 < H < 1$  is the Hurst exponent, and  $\equiv$  means that the variance is the same for both sides of the equation (Feder (1988) (38); Beran 1994 (40); Gilmore et. al. (2002) (41); Hardstone et. al. (2012) (39)). The Hurst exponent provides a measure of the long-term memory of a time series:  $H = 0.5$  indicates an uncorrelated series;  $H > 0.5$  corresponds to a positively-correlated (“persistent”) series in which a positive (negative) fluctuation tends to be followed by a positive (negative) fluctuation;  $H < 0.5$  corresponds to an anti-correlated (“antipersistent”) series in which a positive fluctuation tends to be followed by a negative fluctuation and vice versa. The traditional model for a stochastic nonstationary self-affine process is fractional Brownian motion (fBm) (Mandelbrot & Van Ness (1968) (42)). It is a generalization of the well-known Brownian motion, which is a Gaussian process ( $H = 0.5$ ) with increments that are not independent. Figure 2b presents example of a non-stationary time series in the data which will be analyzed.

The defining property of stationary processes  $X(t)$  is that their statistical properties do not depend on time. A weaker form of stationarity just requires that the mean and the variance are independent of  $t$  (independent of the time period over which these quantities are calculated). Figure 2a presents an example of a stationary time series in the data which will be analyzed. It follows that the self-affinity described by equation (1) is not relevant in this case, since by definition the variance does not change in time. Instead stationary processes can exhibit a type of scale invariance in which the autocorrelation function depends only on the time difference  $\tau$  and satisfies  $r(\tau) \propto \tau^{(2H-2)}$ . The traditional example of these scale-invariant processes is fractional Gaussian noise (fGn), which is a generalization of Gaussian noise ( $H = 0.5$ ). Mandelbrot & Van Ness (1968) (42) showed that the increments of a fBm signal are described by a fGn process. Similarly the cumulative sum of a fGn signal leads to a fBm self-affine process.

## 2.2 Detrended Fluctuation Analysis

Detrended fluctuation analysis (DFA) is a method designed to determine the true scaling properties of a signal by identifying long-term correlations in noisy and nonstationary time series after accounting for external trends (eg. Peng et. al. (1994) (27); Chen et. al. (2002) (28); Hu et. al. (2001) (29); Kantelhardt et. al. (2002) (30)). It has subsequently been shown that DFA can also be used in the analysis of stationary time series, and can therefore be applied without previous knowledge of the time series' statistical properties. It has successfully been applied to diverse fields such as DNA sequences (Peng et. al. (1994) (27)), cloud structure (Ivanova et. al. (2000) (43)), geology (Malamud & Turcotte (1999) (44)), and solid state physics (Kantelhardt et. al. (1999) (45)). Recently DFA has been used in the analysis of CH and QS data (Cadavid et. al. (2019) (26)) and to investigate the long term memory in magnetic field time series measured by the Parker Solar Probe (Dudok de Wit et. al. (2020) (46)).

In order to treat all processes in the same manner and exploit the self-affine properties, it is convenient to define the “profile” of a time series,  $X(k)$ , of length  $N$  as

$$Y(i) \equiv \sum_{k=1}^i (X(k) - \langle X \rangle), \text{ for } i = 1, \dots, N, \quad (2)$$

where  $\langle X \rangle$  is the mean of the time series. By calculating the cumulative sum there is no need to consider whether the time series is stationary or nonstationary before other analysis is performed (Hardstone et. al. (2012) (39)).

After calculating the profile,  $Y$ , for a time series of length  $N$ , the method implements the following steps as described by Kantelhardt et. al. (2002) (30):

The profile is divided into  $N_s = \text{int}(N/s)$  non-overlapping segments of temporal length (scale)  $s$ , and a least-squares method is used to fit a polynomial  $y_v$  of degree  $m$  to each segment  $v$ . The fitted polynomial is then subtracted from each profile segment to obtain the variance

$$F^2(v, s) \equiv \frac{1}{s} \sum_{i=1}^s (Y[(v-1)s + i] - y_v(i))^2. \quad (3)$$

for  $v = 1, \dots, N_s$ . The procedure is repeated for the second case in which the series is divided into



segments starting at the end:

$$F^2(v, s) \equiv \frac{1}{s} \sum_{i=1}^s (Y[N - (v - N_s)s + i] - y_v(i))^2. \quad (4)$$

for  $v = N_s + 1, \dots, 2N_s$ .

The fluctuation function is then given by

$$F(s) = \left( \frac{1}{2N_s} \right) \left( \sum_{v=1}^{2N_s} F^2(v, s) \right)^{1/2}. \quad (5)$$

If the time series has a scaling symmetry, the fluctuation function satisfies the scaling law

$$F(s) \sim s^\alpha \quad (6)$$

The “generalized Hurst exponent”,  $\alpha$ , is then obtained from log-log plots of  $F(s)$  vs.  $s$  for the appropriate scaling range. The exponent  $\alpha$  can then be related to the Hurst exponent and applied to a range of time series with different statistical properties (Mandelbrot & Van Ness (1968) (42); Davis et. al. (1994) (47)). When applying the method we calculate the fluctuation function at equally spaced log(time) intervals up to temporal scale  $s \sim N/3$  before the results become statistically unreliable. For stationary time series,  $0 < \alpha < 1$  and  $H = \alpha$ , while for nonstationary time series,  $1 < \alpha < 2$  and  $H = \alpha - 1$ . Well-known examples of time series are white noise ( $\alpha = H = 0.5$ ), Brownian motion ( $\alpha = 1.5, H = 0.5$ ), and red noise ( $\alpha = H = 1$ ). If the spectral exponent  $\beta < 3$  the time series have stationary increments and  $\beta = 2\alpha - 1$  (Heneghan & McDarby (2000) (48)). Other reference values of interest to solar physics are  $\beta = 5/3 \sim (\alpha = 1.33)$  for Kolmogorov-type turbulence, and  $\beta = 3/2 \sim (\alpha = 1.25)$  for Kraichnan’s model of Alfvén-wave turbulence (Marsch & Tu (1997) (49), and references therein).

Cadavid et. al. (2019) (1) used DFA to investigate the scaling properties of EUV intensity fluctuations of three CHs and adjacent QS regions located near the equator. They found that the signals obeyed a scaling symmetry for a temporal range of  $\sim 20$  to  $\sim 60$  minutes. They generated maps of the generalized Hurst exponent  $\alpha$  and found that in CHs and in the QS sub-regions with open magnetic fields of the dominant polarity, the generalized exponent tended to have values

corresponding to positively-correlated (persistent) processes ( $0.5 < \alpha < 1$ ). In QS regions and in CH sub-regions with magnetic bipoles, the scaling exponent tended to have values corresponding to anti-correlated turbulent-like processes ( $1.0 < \alpha \leq 1.5$ ). They found that near the CH boundaries, the scaling exponent tended to  $\alpha \sim 1$ , which is characteristic of  $1/f$  or red noise.

### 2.3 Multifractal Detrended Fluctuation Analysis

It has been found that in nature many time series do not present a simple monofractal scaling law. In these more complex time series there can be a scaling law for short term scales and another for long term scales. In even more complex cases different scaling exponents may characterize different parts of the time series. This situation is described as if there were many "interwoven fractal" subsets in the time series. To be able to describe the multiple scaling properties of these systems the method of multifractal detrended fluctuation analysis (MF-DFA) was developed (Kantelhardt et. al. (2002) (30)). Time series which exhibit a multifractal structure tend to present both local small and large fluctuations (Ihlen (2012) (50)) as can be seen in the examples presented in Figure 2b.

As described by Kantelhardt et. al. (2002) (30), the multifractality in a time series can have two main origins. It can result from intermittency, "spikiness", in the time series which leads to a broad probability distribution of values with fat tails and deviating from a Gaussian distribution, or the multifractality can be a consequence of long-term correlations. To determine which is the case, the scaling analysis can be applied to a randomly reshuffled version of the time series. If the multifractality is a result of long-term correlations it will disappear for the reshuffled series. When both types of multifractality are present the reshuffled series will show a decrease in the degree of multifractality compared to that of the original time series (Kantelhardt et. al., (2002) (30)).

To characterize the multifractality Kantelhardt et. al. (2002) (30) implements MF-DFA as an extension of DFA in which the variance in equation 4 is generalized to consider both positive and negative moments as follows:

$$F_q(s) = \left( \frac{1}{2N_s} \right) \left( \sum_{v=1}^{2N_s} [F^2(v, s)]^{q/2} \right)^{1/q}, \quad (7)$$

for the case  $q \neq 0$ . For  $q = 0$  the fluctuation function is given by

$$F_0(s) = \exp \left( \frac{1}{4N_s} \sum_{v=1}^{2N_s} \ln [F^2(v, s)] \right). \quad (8)$$

If there is a scale invariance present the fluctuation satisfies

$$F_q(s) \sim s^{h(q)}. \quad (9)$$

Kantelhardt et. al. (2002) (30) considers that for large scales,  $s > N/4$ , the results become statistically unreliable because of the low number of cases in the sum. In the present project the focus is on the fluctuations of the time series, so there will be also be a minimum temporal scale to avoid effects of the 5 minute oscillation which is ubiquitous in the Sun. The function  $h(q)$  is the “generalized Hurst exponent” obtained from log-log plots of  $F_q(s)$  vs  $s$  for the appropriate scaling range. For  $q = 2$  the analysis corresponds to the DFA calculation with  $h(2) = \alpha$  (Figure 3).

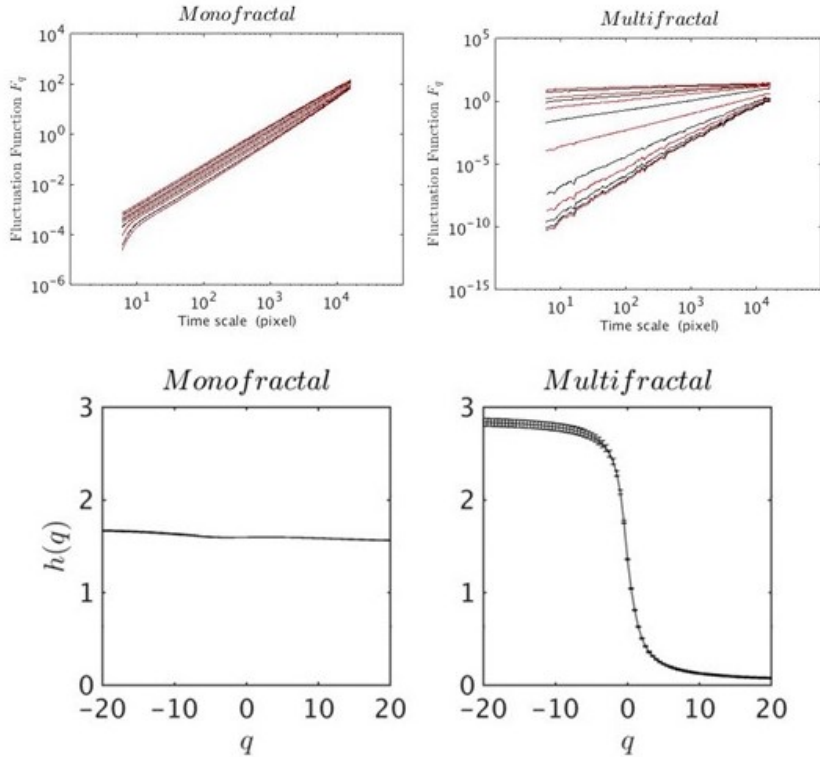


Figure 4: Fluctuation function vs scale and generalized Hurst exponent vs moment for artificial data. Left panels: monofractal. Right panels: multifractal.

Since the this project will make extensive use of the values of these exponents to characterize the data the classification in terms of the Hurst exponent is reviewed. For stationary time series, including fGn,  $0 < h(2) < 1$  and  $h(2) = H$ . For fBm type process,  $1 < h(2) < 2$  and  $H = h(2) - 1$  (Heneghan & McDarby, (2000) (48); Mohaved et. al. (2008) (51)).

As shown in Figure 3, for a monofractal times series  $h(q)$  is constant and independent of  $q$  (however see discussion in the next paragraph dealing with spurious multifractality). For a “text-book” multifractal,  $h(q)$  is a decreasing function of  $q$  that tends to constant values asymptotically for both positive and negative moments. For this approach, the standard definition of the degree of multifractality is given by  $\Delta h = h(q_{min}) - h(q_{max})$  (Figure 4). The order of  $q$  weights the influence that the fluctuations have in the calculation of the fluctuation function. The scaling properties of the small fluctuations are described by the negative  $q$  moments while the scaling properties of the large fluctuations are described by the positive  $q$  moments. When noise with small amplitude is added to a signal its presence primarily affects the generalized exponents on the negative side. An ideal monofractal would give  $\Delta h = 0$ . In practice the limited length of the time series causes a small spurious multifractal effect for a monofractal time series (Grech & Pamula (2013) (52)). To minimize this effect it is recommended that a time series should have at least  $2^{10}$  temporal pixels. A way to account for this error is to calculate the degree of multifractality for a times series of Gaussian noise with the same length as that of the data and subtract this value from the  $\Delta h$  found for the data.

## 2.4 The Effect of Noise

The intensity time series investigated in this project include a certain percentage of uncorrelated observational noise. This noise is typically modelled by a Gaussian or Poisson distribution and corrections are implemented to “subtract” these contributions from the signals. Since the focus of the present analysis are the fluctuations of the time series at all temporal scales, such subtraction is not advisable because it may also take out information from the actual stochastic signal. The only path forward is to interpret the results by taking into account the contributions from the observational noise, as will be shown.

Ludescher et. al. (2011) (53) have precisely investigated the performance of MF-DFA when applied to simulated multifractal time series when white noise of varying amplitude is added. They first generated a multifractal signal  $\bar{X}_i$  via a variant of the well known multiplicative random cascade (MRC) process (Feder (1989) (54)). To this signal they added a white noise series  $U_n$  of zero mean and unit variance:

$$X_i = \bar{X}_i + A U_i \quad (10)$$

where  $A$  defines the amplitude of the noise. The authors investigated the average over 100 time series of 256 pixels in length.

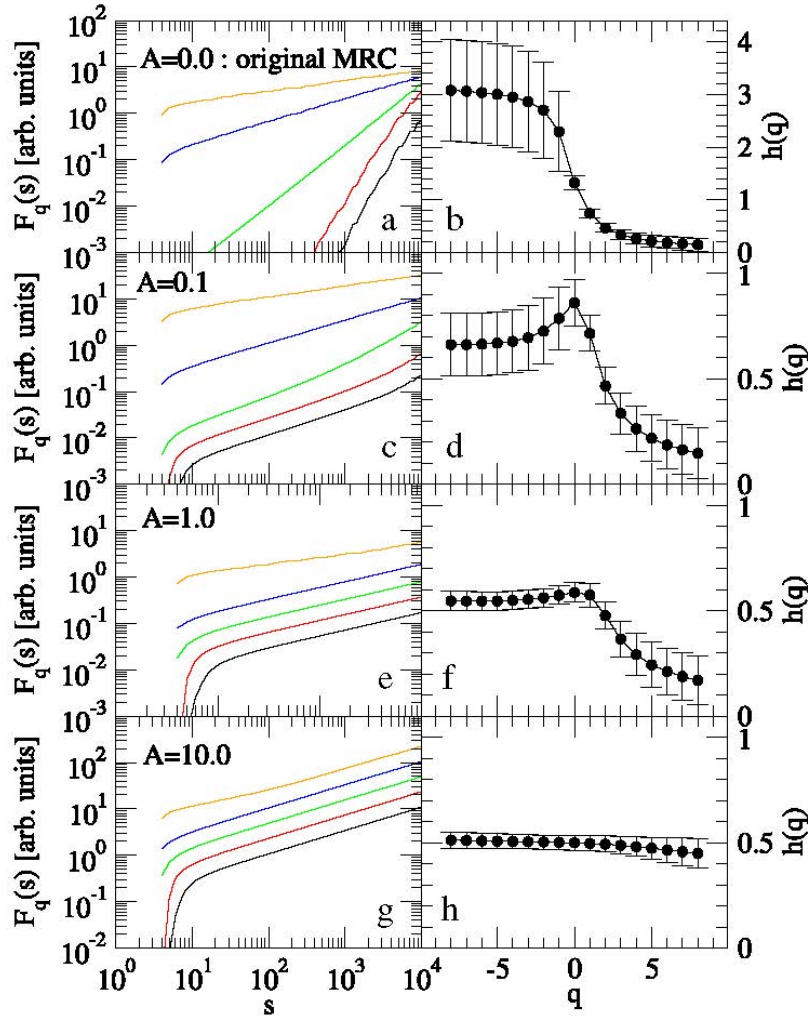


Figure 5: Fluctuation functions  $F_q(s)$  (left) and generalized Hurst exponents  $h(q)$  (right) for multifractal time series with added white noise of zero mean, unit variance, and amplitude  $A$ . The scaling exponents are calculated for the large scale range  $10^3 < s < 10^4$ .  $A = 0$  (a) and (b).  $A = 0.1$  (c) and (d).  $A = 1.0$  (e) and (f).  $A = 10$  (g) and (h). From Ludescher et. al. (2011) (53).

Figure 5 (left) displays  $F_q(s)$  vs  $s$  for the four cases with amplitudes  $A = 0, 0.1, 1.0, 10$ . The left panels display the corresponding  $h(q)$  vs  $q$  curves. For moderate levels of noise the  $h(q)$  for  $q < 2$  is affected showing a decrease (panels *d* and *f*) even displaying a section of "reversed" multifractality where  $h(q)$  increases with increasing  $q$ . The  $h(q)$  with  $q > 2$  remains almost unchanged. For a large noise amplitude (panel *h*) the noise signal dominates and the generalized exponent tends to the monofractal curve which characterizes the white noise signal with  $h(q) = H = 0.5$  for all  $q$ .

## 2.5 Potential Magnetic Field Extrapolation

The magnetic field observations available for the present project consist of line-of-sight (LOS) observations at the solar photosphere. In order to find insight into the 3-dimensional structure of the magnetic fields at higher levels of the atmosphere it is necessary to perform a current free potential field extrapolation. This approximation is valid because the effects of currents are expected to have meaningful effects for long ( $\sim 100$  Mm) coronal loops in active regions but not for open-field lines and short closed loops which characterize the CH and QS regions (Wielgelmann & Solanki (2004) (55)). The extrapolation is implemented with the IDL routine `lff extrapol.pro` by M.K. Georgoulis which is based in the Fast Fourier method developed by Alissandrakis (1981) (56).

## 2.6 k-means Clustering

As described in the introduction, 190 cases are investigated in this study. To organize the results and extract meaningful information which can be related to physical structures or processes the k-means clustering algorithm is applied.

k-means (Lloyd (1982) (57), Forgy (1965) (58)) is one of the machine learning iterative algorithms used to partition data sets into clusters. Each cluster is defined by a centroid and a data element belongs to the cluster with the nearest mean distance to the centroid. In its simplest form, the "k-means algorithm", or Lloyd–Forgy algorithm, randomly chooses  $k$  observations from the data set that identifies as centroids  $(c_1^{(1)}, c_2^{(1)}, \dots, c_k^{(1)})$  where the superscript (1) denotes the first iteration. Then each observation is assigned to the cluster with the nearest centroid, determined by the least squared Euclidean distance between observation,  $x_p$ , and centroid:

$$S_i^{(t)} = \{x_p : \|x_p - c_i^{(t)}\|^2 \leq \|x_p - c_j^{(t)}\|^2 \ \forall j, 1 \leq j \leq k\} \quad (11)$$

where  $(t)$  is the iteration number.

Then the positions of the centroids are recalculated based on the elements of the cluster

$$c_i^{(t+1)} = \frac{1}{|S_i^{(t)}|} \sum_{x_p \in S_i^{(t)}} x_p \quad (12)$$

where  $|S_i^{(t)}|$  is the number of elements in  $S_i^{(t)}$ .

The two steps are repeated until the assignments of the observations to the clusters do not change. To select the number of initial centroids it is possible to make *educated guess* for data sets with a small numbers of attributes/characteristics. However this is challenging when the number of possible clusters is large. In the present study the Elbow method (Thorndike (1953) (59)) was used as a guide but ultimately knowledge of the data set informed the choice.

There is no guarantee of finding an optimum result. There are a variety of initialization methods which can give better results depending on the type of data, as well as variations on the calculation of the centroids and the iterations. This project uses the Python KMeans algorithm in the scikit-learn library of subroutines.

To better visualize the results in a three-dimensional parameter space convex hulls (convex envelopes) over the cluster points were calculated. Considering a bounded subset of points in the plane, the convex hull can be visualized as the shape enclosed by a rubber band stretched around the outer points of the subset. To implement this calculation the subroutines ConvexHull and Delaunay from the SciPy library of subroutines were used.

### 3. Data and Data Preparation

#### 3.1 Description of the Data

This study uses EUV intensity images in the 171 Å, 193 Å, and 211 Å wavebands, observing temperatures of  $\sim 0.7$  MK,  $\sim 1.2$  MK, and  $\sim 2.0$  MK respectively (Garton et. al. (2018) (60)), obtained with the AIA instrument (Lemen et. al. (2012) (61)) onboard the SDO spacecraft (Pesnell et. al. (2012) (62)). The temporal cadence is 12 seconds and the pixel scale of  $0.6''$  ( $\sim 0.44$  Mm). This project uses 5 hours (1500 temporal pixels) of data of an equatorial CH located near disk center which was observed on 16 April 2017 starting at 12:00:00. This case was selected because the CH has a clear boundary which tends to preserve its structure during the time period studied, making it ideal for long range temporal analysis studies like MF-DFA. The scaling analysis was performed on a data cube analyzed is centered at  $(33.4'', 57.97'')$  with a field of view of  $(400'', 520'')$ . It was obtained via the Joint Science Operation Center (JSOC) Cutout Service selecting the “tracking” option which accounts for the solar rotation by tracking the image patch at the Carrington rate. The images were coaligned by using the central image in the time series as a reference. As described below, one of the methods applied to define the CH boundary uses full disk images in the 171 Å, 193 Å, and 211 Å wavebands at the time of the reference image. Full disk images of these wavebands were obtained using Sunpy.net Fido routine, aligned using the aiapy.calibrate register method, and finally cut into sub-maps using the previously mentioned arc-second center and field of view for the respective data cube. Contemporaneous LOS magnetic field density images were obtained with the HMI instrument (Schou et. al. (2012) (63)) onboard SDO, was used to provide the magnetic boundary context and to derive the potential field extrapolations. In the former case, the full disk magnetic image was obtained via Sunpy.net Fido routines and aligned using Sunpy’s reproject\_to method with respect to the previously mentioned 171 Å image after it was transformed to a level 1.5 image using the aiapy.calibrate register method. In the latter case, the full disk magnetic image is re-scaled and co-aligned with respect to the 193 Å full disk reference image using the IDL routine aiaprep.pro.

Figure 6a displays the 193 Å intensity reference image and Figure 6b the corresponding mag-



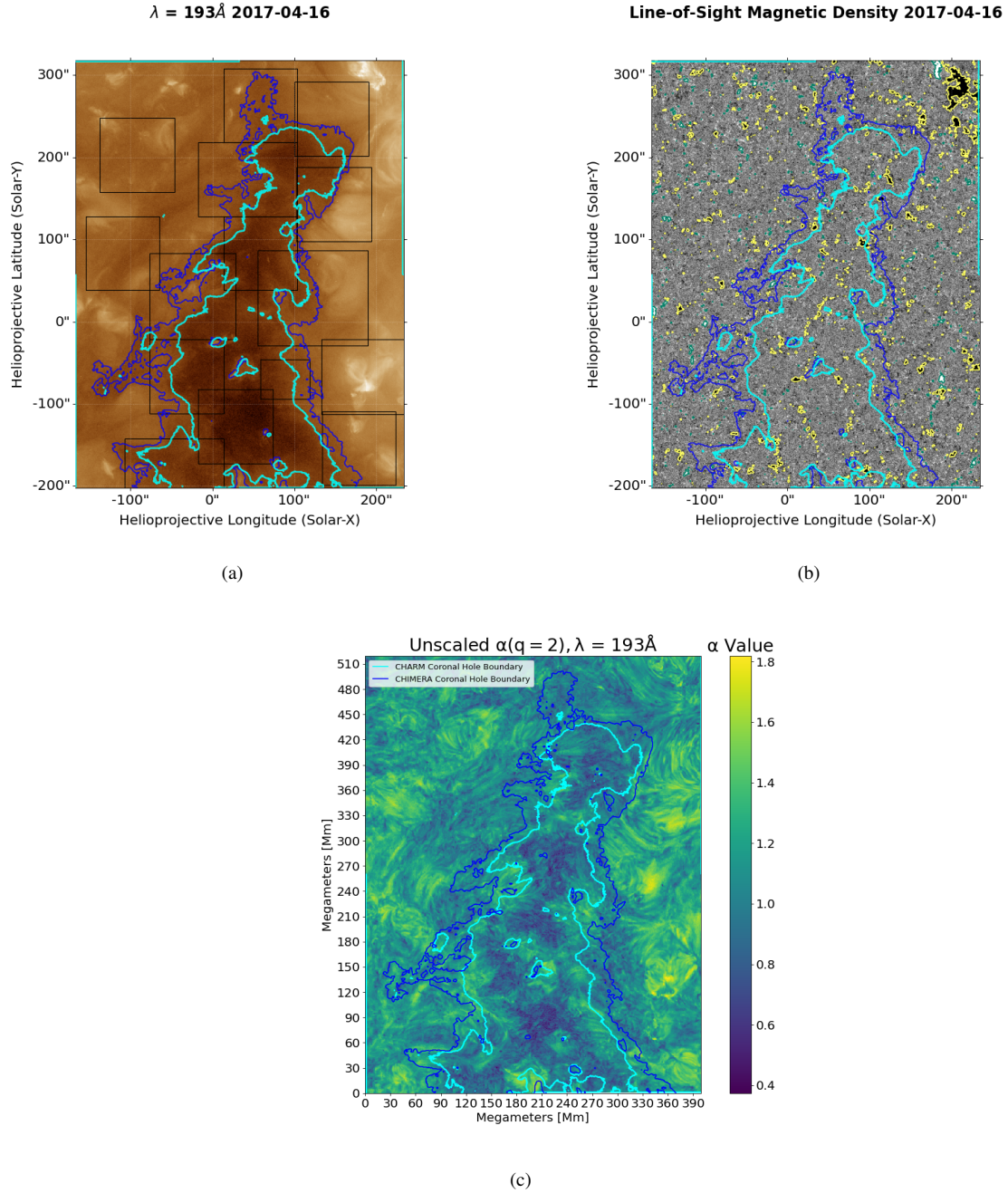


Figure 6: Three figures depicting the data before, and after analysis. (a) AIA 193A image of the CH used in the creation of the CHIMERA boundary. Fifteen boxes within the figure define the regions used for the MF-DFA analysis. (b) Contemporaneous LOS HMI image used in the creation of the magnetic field boundaries. (c) Unscaled  $\alpha$  map created via the DFA.

netic field image, both obtained using the Sunpy.net Fido routine. The 15 sub-regions investigated in the MF-DFA analysis are indicated by the rectangular back boxes in Figure 6a. The CH boundary calculated by the CHARM and CHIMERA methods is displayed over all three images in picture 6 with CHIMERA being the dark blue boundary and CHARM being the light blue boundary.

### 3.2 Defining a Coronal Hole Boundary, CHARM and CHIMERA

Because of the relation between CHs and the solar wind, there is great interest in their automatic detection and the identification of their properties. Of particular interest is the relation between the CH area the high-speed solar wind peak velocity at the Earth’s location (Samara et. al. (2022) (64)). Reiss et. al. (2021) (65) have performed a comparison of nine automated detection mechanisms and finds that there is no consensus on the identification of the CH boundary. With this result in mind this project uses two different methods to define the CH boundary and explores how the properties vary in the region between the two boundaries.

The first method is adapted from the CHARM algorithm (Krista & Gallagher 2009 (66)). An average image is calculated by taking the mean of every other 50th image in the data-cube of 193 Å intensities. A histogram of the average intensities presents a minimum value which indicates the possible threshold dividing the CH from the QS intensity distributions. Starting with this value as a guide the intensity threshold is manually changed until the boundary on the average image separates the QS intensities and the darker pixels corresponding to the CH.

In contrast to the CHARM approach, which uses only the 193 Å data, the multi-thermal emission recognition algorithm (CHIMERA) implements an intensity segmentation of the data using three EUV wavebands (171 Å, 193 Å, and 211 Å) (Garton et. al. (2018) (60)). This method considers two dimensional histograms in pairs of the analyses’ three wavebands and segments the pixels with the low intensities corresponding to a CH. Next, it uses the information from a contemporaneous magnetogram to exclude smaller sub-regions that do not have the unipolar properties of CHs (Garton et. al. (2018) (67)). The original code was developed in IDL and is shared with the community via GitHub. For the present project the code was re-written, for the most part, in Python. The automated process uses SunPy routines to gather the level 1 intensity and magnetic

data from the JSOC repository, and co-aligns it using aiaPY to produce the level 1.5 images which are then fed to the newly developed code.

The the images in Figure 6 display the CH boundaries calculated with the CHARM and CHIMERA methods. In the subsequent analysis, three regions will be considered. The inside of the CH is henceforth defined by the area inside the CHARM boundary, while the area outside of the CHIMERA boundary is defined as the outside of the CH or the QS region. Finally the area inside of the CHIMERA boundary, but outside of the CHARM boundary is defined as the in-between region.

### 3.3 Defining Magnetic Field Boundaries

Standard Python Matplotlib routines were used to create a boundary for the observable magnetic network which are used in defining regions with magnetic activity. The images used in the creation of the magnetic network boundaries were obtained by the previously mentioned Sunpy.net Fido routines. The cutoff for defining the boundary of the magnetic network was set at 33 G. Selected pixels that fall within the boundaries that define the magnetic network are henceforth referred to as selections with magnetic activity. Figure 6b displays the magnetic field reference image with the network boundary pixels indicated in yellow.

## 4. Results

### 4.1 Analysis Strategy and Case Selection

The original code implementing the MF-DFA analysis in Python was obtained through GitHub and slightly altered to include the  $q=0$  moment. Because of the observational noise in the data, it is necessary to calculate the average multifractal spectrum for a collection of pixels. Based on results in the scientific literature and through experimentation it was decided that an appropriate number would be around 100 pixels. A collection of pixels of which the average multifractal spectrum was calculated across constituted a case. A majority of these cases were selected through rigid rectangular boxes in an attempt to treat each of the cases on equal conditions.

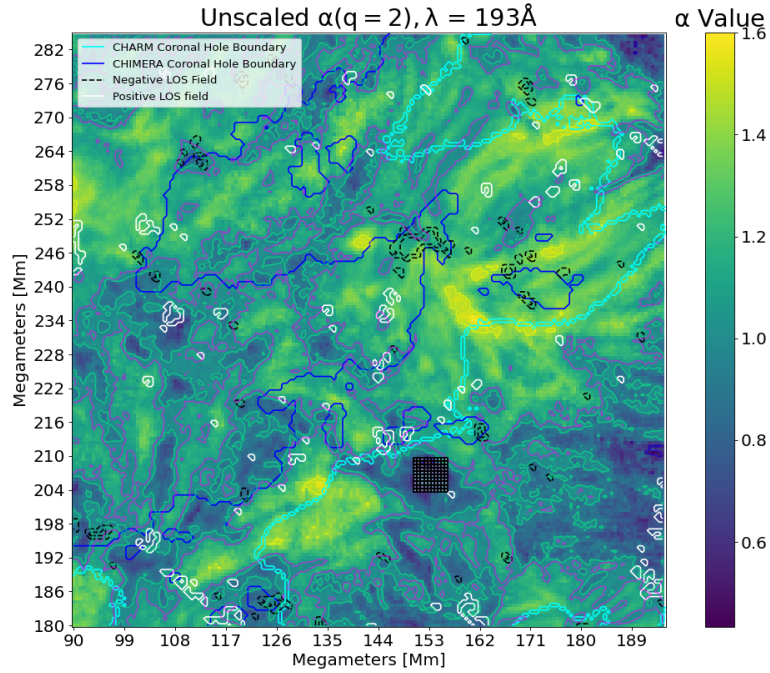


Figure 7: The above image exemplifies the process of selecting a case. The image is of the unscaled  $\alpha$  values obtained over each pixel in the sub-region. The boundaries of the CHARM, CHIMERA, and magnetic network are seen overlaid. Pixels are shown being selected with which the average multifractal spectrum is calculated across.

The strategy followed was to first select 15 main sub-regions, displayed by the black rectangular boxes in Figure 6a, and calculate for each pixel within them the fluctuation functions for 21 values of  $q$  ranging between -10 and 10. The sizes of the regions were limited by the memory available

in the server to perform the calculations over the large data-cubes.

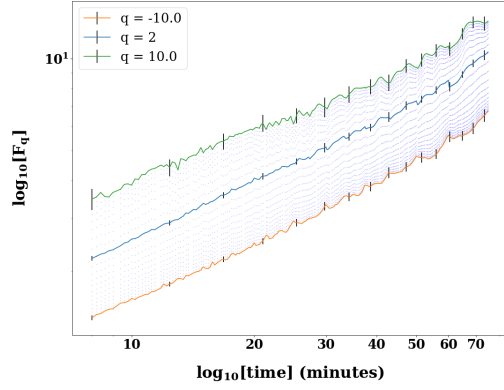
The second step was to calculate the values of the exponent,  $\alpha = h(2)$ , for all the pixels in the image using the full range of temporal scales to calculate the slopes that give the exponents. The entire "unscaled"  $\alpha$  map is displayed in Figure 6c. The unscaled  $\alpha$  map was further enriched by adding the CHARM and CHIMERA boundaries as well as the contours for the network fields distinguishing the positive and negative polarities. Figure 7 displays the complete unscaled  $\alpha$  map for one of the 15 sub-regions.

A Python program was written which loads the previously calculated fluctuation functions for one of the 15 sub-regions. By viewing the unscaled  $\alpha$  map, the user manually selects the pixels of interest to define a case to be studied. An example of a case is shown in picture Figure 7 represented by the black grid centered at about (152 Mm, 206 Mm), in which it is seen that the selected pixels have values of  $\alpha < 1.0$ , are inside CH, and are not near the magnetic network. The fluctuation functions of the selected pixels are then averaged across temporal scales, which reduces the uncorrelated observational noise and enhances the possibility of identifying a scaling symmetry. The program displays the averaged fluctuation functions vs temporal scale, and the user can inspect what is the possible scaling range for each moment  $q$ , three examples of which are shown in figure 8 (left). The scaling range used to calculate the slope corresponding to the generalized Hurst exponents,  $h(q)$ , is finally defined by taking in consideration the limits of the  $q = -10$  and  $q = 10$  cases in which the scaling range is more limited. The program then finally calculates the degree of multifractality  $\Delta h = h(-10) - h(10)$ , shown in figure 8 (right).

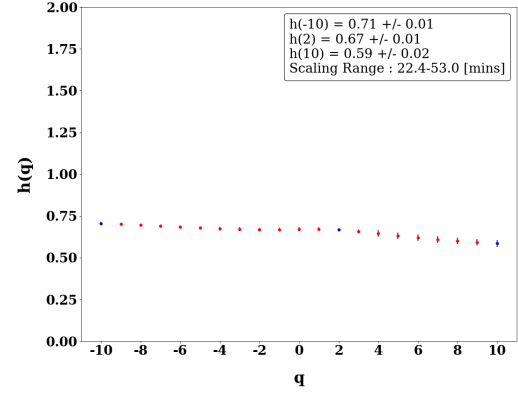
To further account for the effects of white noise the average multifractal spectrum was calculated for a 100 strings of length 1500 pixels of randomly generated white noise. This gave a spurious degree of multifractality  $\Delta h_{sp} = 0.13$ . If the multifractality of the case after subtraction of the spurious multifractality is greater than 0.10, the case is deemed to be a multifractal.

## 4.2 Exploration of the Data Set

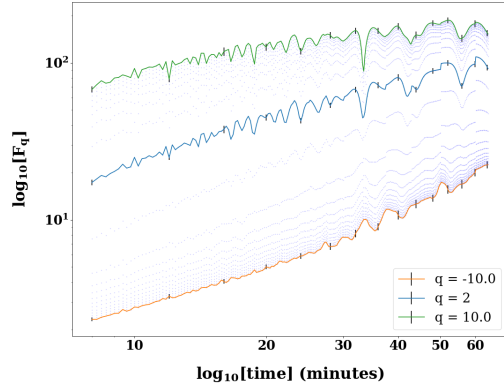
Because it is impossible to know apriori whether there is a scaling symmetry, and if it is present, what the scaling range is, the analysis cannot be automatized and the user has to define a case by



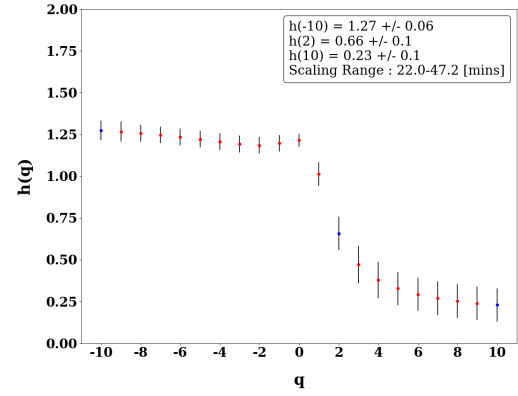
(a)



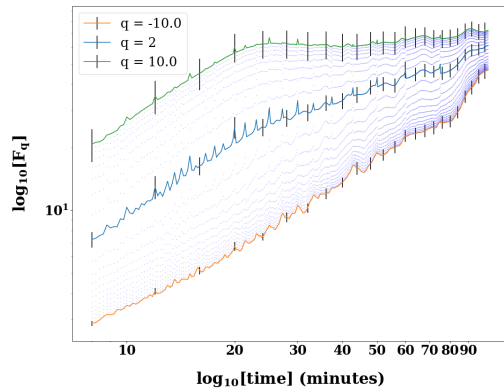
(b)



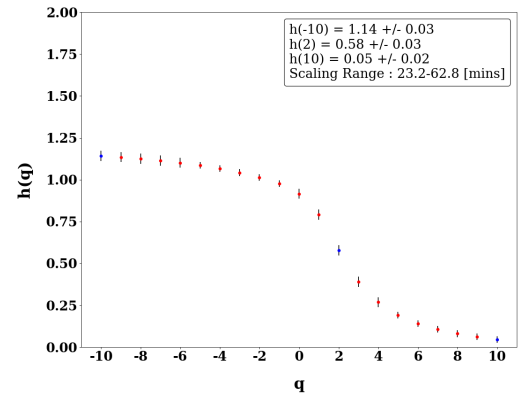
(c)



(d)

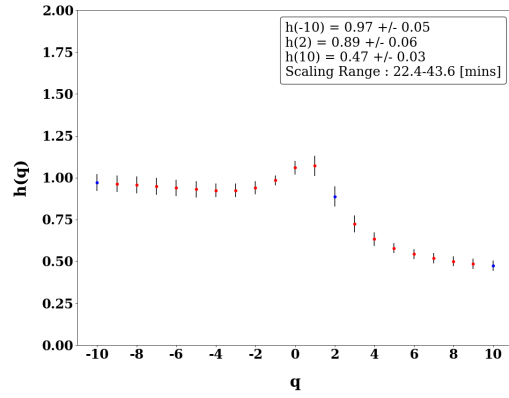


(e)

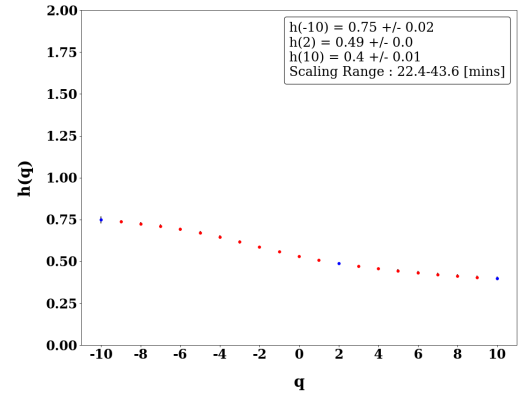


(f)

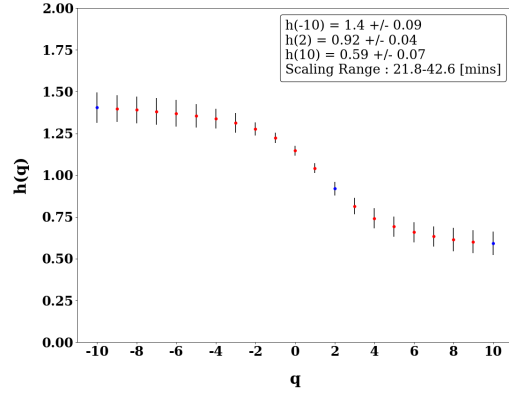
Figure 8: Three sets of figures depicting an example of a monofractal, (a) and (b), multifractal with noise, (c) and (d), and a multifractal, (e) and (f), obtained from the data set.



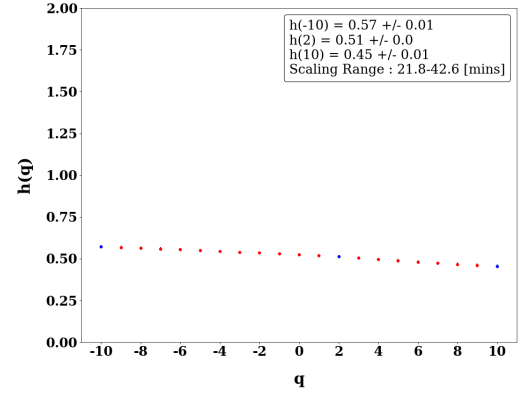
(a)



(b)



(c)



(d)

Figure 9: Four figures showing the effect of the reshuffling process. (Left) The original time series. (Right) The reshuffled time series. The top series remains multifractal after reshuffling due to intermittency in the time series.

manually selecting the pixels associated with particular features or structures in the unscaled  $\alpha$  map.

A total of 190 cases were investigated by sampling inside, outside, and the region in between the two boundaries of the coronal hole. Figure 8 displays three examples of the fluctuation functions vs temporal scale and the corresponding spectrum of generalized exponents for representative cases displaying a monofractal (a), a noisy multifractal (b) and a multifractal (c). The scaling ranges are in the order  $\sim 11 - 40$  minutes for all of the cases. Cases like the ones displayed in figure 8 are encountered inside, outside, and in between the coronal hole boundaries.

Figure 9 presents two multifractal cases before and after the random shuffling of the time series. In case 1 (top) the multifractality remains albeit reduced. This corresponds to a situation in which the underlying signals present long term correlations and also intermittency. In case 2 (bottom) the multifractality disappears, indicating that its origin could be attributed only to the long term correlation in the emission process.



## 5. Summary and Discussion of Results

### 5.1 3-Dimensional Parameter Space: Initial Classification

The results of the MF-DFA on the 190 cases depend on the generalized Hurst exponent  $\alpha$  and the degree of effective multifractality  $\Delta H - H_{sp}$ . For each of the cases it was also determined if the pixels included part of the network fields. To complement this analysis the flux imbalance for the LOS magnetic field  $B_i$  was calculated as the ratio of the sum of the signed fields to the sum of the unsigned fields:

$$\zeta = \frac{\sum_i B_i}{\sum_i |B_i|} \quad (13)$$

where the sum is taken over all pixels for a given case.

If a threshold for the flux imbalance is set at 0.6, with network regions characterized by  $\zeta > 0.6$ , it was found that 183 (96 %) of the cases were correctly classified by the value of the flux imbalance, justifying its use as a proxy for deciding whether a region has or not a prevalence of network fields.

The results are summarized in Figure 10 (top-left) using the three dimensional parameter space determined by  $\alpha$  (x-axis),  $\Delta H - H_{sp}$  (y-axis) and  $\zeta$  (z-axis).

The cases inside the CH are depicted in blue, those outside the CH corresponding to the QS in orange, and the ones in the “in-between” region defined by the the two boundaries are in black. As an initial attempt to make sense of the results, two-dimensional projections are presented in the remaining panels of Figure 10 with thresholds for the three parameters as follows:  $\alpha = 1$  separating the persistent (below) from the anti-persistent (above) cases;  $(\Delta H - H_{sp}) = 0.1$  separating the monofractal (below) from the multifractal (above) cases;  $\zeta = 0.6$  separating the regions associated with the network (above) and without network pixels (below).

The number of pixels in each of the quadrants  $Q_i$  (counterclockwise with  $i = 1$  at top-right) of the two dimensional cuts corresponding to the three physical regions, inside the CH, outside the CH and in between the boundaries, are summarized in Table 1. Some of the more notable results follows. Figure 10 (top-right) indicates that 78 (41 %) of the cases are persistent and multifractal. Of these 46 % are inside the CH and 33 % in the QS region. Also 25 % of the cases are anti-

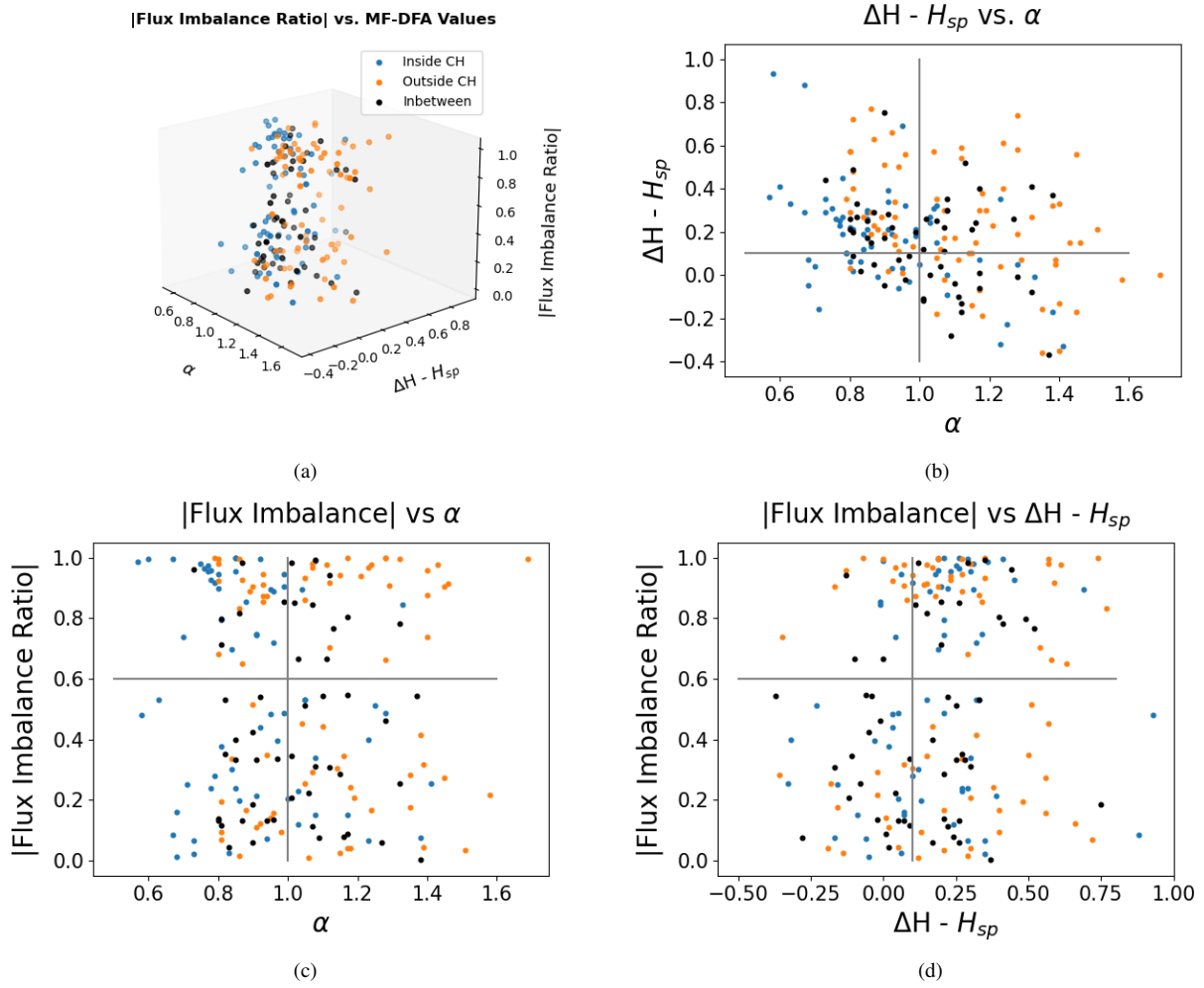


Figure 10: Summary of results for the 190 cases. Top-left: the three parameter space. Top-right: projection onto the  $\Delta H - H_{sp}$  plane. Bottom-left: projection onto the  $\zeta$  vs  $\alpha$  plane. Bottom-right: projection onto the  $\zeta$  vs  $\Delta H - H_{sp}$  plane.

Classification of Results for the Original Time Series

Figure 10	Quadrant	Inside	Outside	In-between	Total Cases
(b)	Q1	7	27	14	48
	Q2	36	26	16	78
	Q3	12	3	7	22
	Q4	10	18	14	42
(c)	Q1	3	24	10	37
	Q2	27	16	6	49
	Q3	21	13	17	51
	Q4	14	21	18	53
(d)	Q1	25	30	13	68
	Q2	5	10	3	18
	Q3	17	11	18	46
	Q4	18	23	17	58

Table 1: Table depicting the number of cases from each region in each quadrant for the respective graphs.

persistent and multifractal with 57 % of them in the QS region. Figure 10 (bottom-left) shows that 53 (27 %) of the cases are anti-persistent and not in the network regions. Of these, 26 % are inside the CH. In contrast 26 % are persistent and in the network and of these 55 % are inside the CH. Figure 10 (bottom-right) indicates that 68 (36 %) of the cases are multifractal and in the network, with 37 % (44 %) inside (outside) the CH. These initial analysis confirms the prevalence of persistent signals inside the CH and anti-persistent signals outside. It suggests a general tendency for the multifractal and persistent cases to occur inside the CH and the multifractal and anti-persistent cases to be in the QS. Of the cases between the boundaries, 45 % are persistent and 55 % are multifractal indicating that this is indeed an “in-between” region. Regarding the classification including the flux imbalance the results are not clear.

It is apparent that there is a need to organize the data in a manner that includes a more insightful classification in the three-dimensional parameter space.

## 5.2 3-Dimensional Parameter Space: k-means Clustering

To gain insight into the results the k-means algorithm has been applied to the data set consisting of 190 cases in a three-dimensional parameter space corresponding to the three “attributes”  $\alpha$ , multifractality, and  $\zeta$ . The Elbow method suggested three clusters but by inspection of the results it was concluded that  $k = 4$  clusters better organized the information. The Python routine used the k-means++ algorithm for the centroid selection which improves the running time.

Figure 11 (top-right) displays the four clusters: 0 (67 (35 %) cases; 1 (55 (29 %) cases; 2 (24 (13 %) cases; 3 (44 (23 %) cases, together with the corresponding convex hulls and centroids. The other three panels display the two-dimensional projections as in Figure 10 but now the points are identified according to the cluster classification and not the physical regions. Tables 2 and 3 summarize the results considering these two approaches to organize the information. The two bottom figures show the clearest correspondence between the clusters and the parameters. Cluster 0 (blue) is primarily characterized by network cases ( $\zeta > 0.6$ ), persistent dynamics ( $\alpha < 1$ ) and multifractality. Cluster 2 (green) is primarily characterized by network cases, anti-persistent dynamics and no multifractality. Cluster 1 (orange) is primarily characterized by non-network cases, persistent

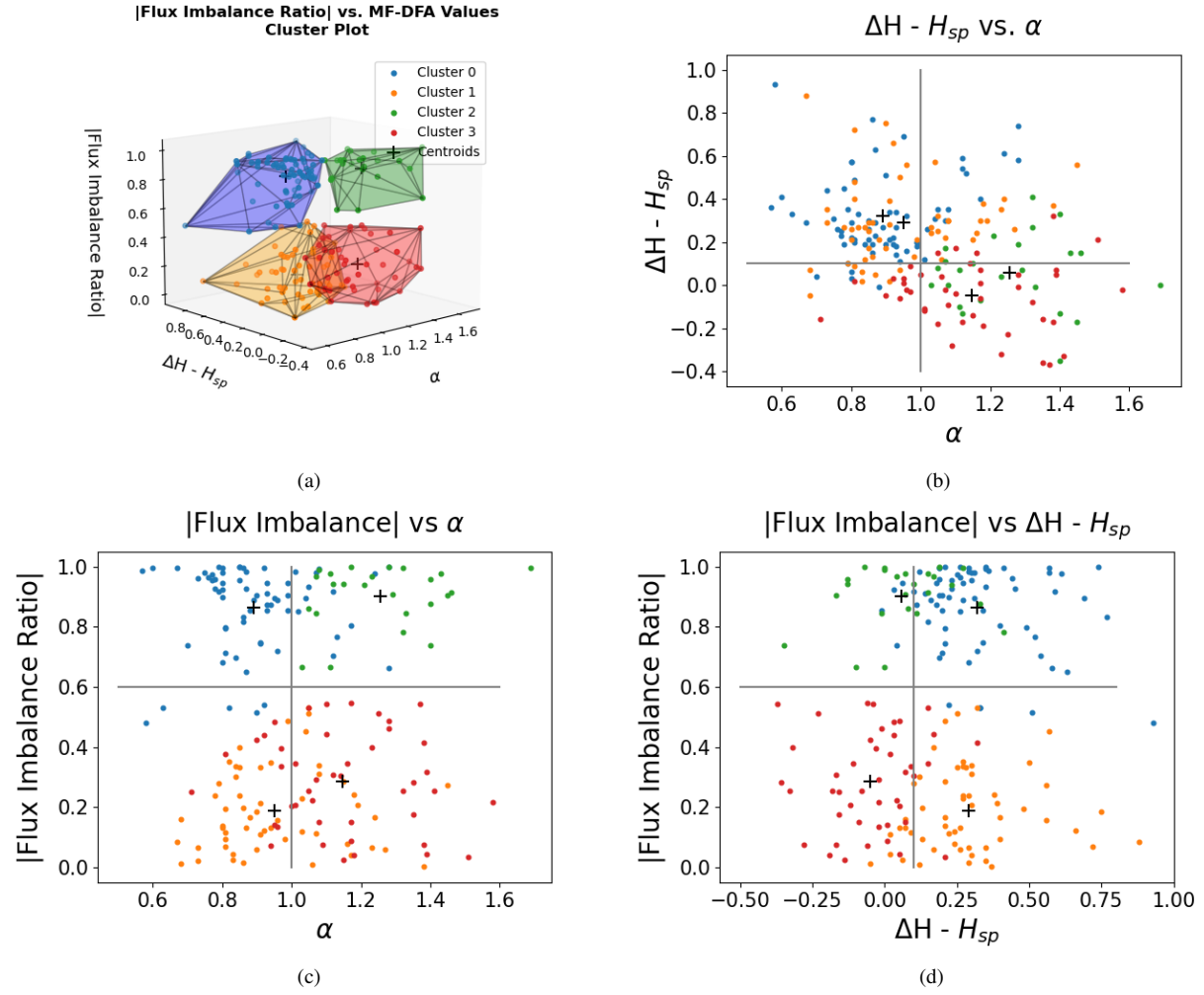


Figure 11: Summary of results for the 190 cases after the K-means clustering algorithm is performed. Top-left: the clusters in three parameter space. Top-right: projection onto the  $\Delta H - H_{sp}$  plane. Bottom-left: projection onto the  $\zeta$  vs  $\alpha$  plane. Bottom-right: projection onto the  $\zeta$  vs  $\Delta H - H_{sp}$  plane.

Classification of Results for the K-Means Clusters 1					
Cluster #	Analysis Method	Inside	Outside	In-between	Total Cases
Cluster 0	# of Cases	30	24	13	67 (35%)
	% of cluster members in region	45	36	19	
Cluster 1	# of Cases	18	18	19	55 (29%)
	% of cluster members in region	33	33	35	
Cluster 2	# of Cases	2	17	5	24 (13%)
	% of cluster members in region	8	71	21	
Cluster 3	# of Cases	15	15	14	44 (23%)
	% of cluster members in region	34	34	32	

Table 2: Summary of results classified according to the number of elements in a cluster in a given region.

Classification of Results for the K-Means Clusters 2						
Region	Analysis Method	Cluster 0	Cluster 1	Cluster 2	Cluster 3	Total Cases
Inside	# of Cases	30	18	2	15	65 (34%)
	% of region cases in cluster	46	28	3	23	
Outside	# of Cases	24	18	17	15	74 (39%)
	% of region cases in cluster	32	24	23	20	
In-between	# of Cases	13	19	5	14	51 (27%)
	% of region cases in cluster	25	37	10	27	

Table 3: Summary of results classified according to the number of cases in a region in a given cluster.

dynamics and multifractality. Cluster 3 (red) is primarily characterized by non-network cases, anti-persistent dynamics and no multifractality. While the separation of the cluster properties using the rigid parameter thresholds is exact only in the case of the flux imbalance ratio, as shown in the Figures 11 (bottom), this approximate division captures in large part the general tendencies of the clusters and will be used in the subsequent analysis.

Based on the results in Table 2, among the network cases: in Cluster 0 (persistent, multifractal) 45% of the cases are inside the CH and 36 % in the QS region; in Cluster 2 (anti-persistent, not multifractal) 71 % of the cases are in the QS region. Among the non-network cases: in Cluster 1 (persistent, multifractal) and Cluster 3 (anti-persistent, not multifractal) the three physical regions are equally represented with  $\sim 33\%$  of the cases each. These results indicate that multifractality tends to be associated with persistent cases and not multifractality with anti-persistent cases. The network regions tend to be multifractal in the CH and not multifractal in the QS. For the non-network these seems to be no relation to the physical regions.

Viewing the data from the point of view of the physical regions (Table 3), 46 % of the cases inside the CH are in Cluster 0 (network, persistent, multifractal) and only 3 % are in Cluster 2

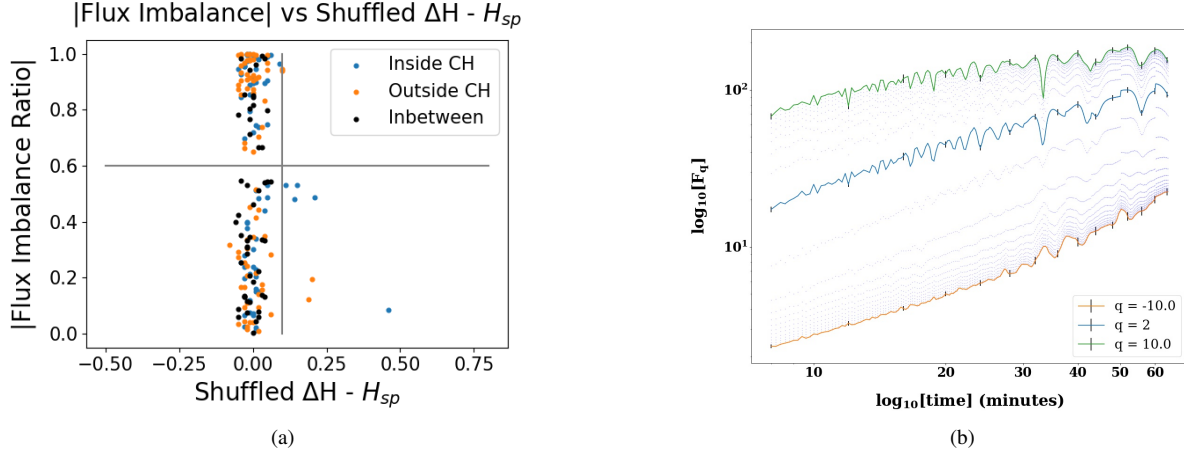


Figure 12: Figure (a) depicts the flux imbalance ratio versus the reshuffled reduced multifractality. Figure (b) shows the not shuffled fluctuations of the case which had the largest degree of multifractality after reshuffling.

(network, anti-persistent, not multifractal). For the non-network clusters 1 and 3 the percentages of CH cases is comparable with 28 % in Cluster 1 and 23 % in Cluster 3. For the cases in the QS region 32 % of the cases are in Cluster 0 (network, persistent, multifractal) and 23 % are in Cluster 2 (network, anti-persistent, not multifractal). For the non-network clusters 1 and 3 the percentages of QS cases is comparable with 24 % in Cluster 1 and 20 % in Cluster 3. For the region between the boundaries, with a lower number of cases, the classification into the clusters gives less distinct results. Among the network fields about double of the cases tend to be (persistent, multifractal) in Cluster 0 as compared to (anti-persistent, not multifractal) in Cluster 2. A slight majority of the cases (65 %) are not in the network and have a slight higher number in Cluster 1 (persistent, multifractal) as compared to Cluster 3.

### 5.3 Reshuffled Time Series and Upsurges

When the signals are reshuffled the generalized Hurst exponent tends to 0.5, reflecting the randomness of these time series. Figure 12 (right) displays the fluctuation functions for one of the sub-regions in which the multifractality remains. Using the same scaling range as for the original time series the new degree of multifractality was calculated. Figure 12 (left) summarizes the results in a plot of flux imbalance ratio vs multifractality. Out of the 190 cases only 7 preserve the multifractality with 5 cases in the CH and 2 cases in the QS. Of these 6 out of 7 are found

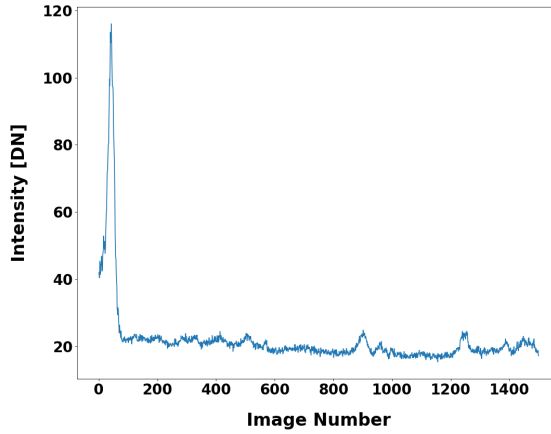


Figure 13: Image displaying an example of a large spiking event in which the MF-DFA method failed to determine the long-range correlations of the time series due to intermittency. The pixels gathered are from a long lasting solar storm in the coronal hole that had ended at the beginning of the time series.

outside the network. The result indicates that in general the multifractality is due to the long range temporal correlations in the time series and not from the intermittency. The fact that the intermittent cases are primarily found in the regions without network fields suggests a different underlying mechanism for the emission.

In the highly dynamic solar environment the intensity observations present evidence of many different processes. There are examples of time series with large intensity upsurges which last for a short time on a background of small fluctuations (Figure 13). In this case there the MF-DFA analysis is not appropriate since the upsurge dominates the statistics and there is no natural scaling range for all the values of  $q$ . When the time series is reshuffled the contributions to the upsurge are randomly distributed throughout the time series and the reshuffled series presents multifractal properties. The origin of this multifractality being the effective intermittency of the reshuffled time series. This is a result which merits exploration in a future study.

Excluding the cases with upsurges, which could possibly be jets, the picture that emerges from this study is that in the CH the large majority (94 %) of the cases in the network regions (32 total cases in Clusters 0 and 2) are (persistent, multifractal). An example of a potential field extrapolation of one these regions inside the CH is shown in Figure 14, with the selected pixels for the MF-DFA indicated in red. The extrapolation displays open fields and large loops, which must

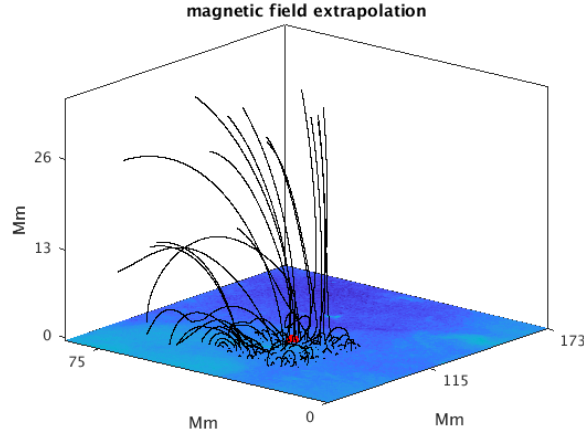


Figure 14: Example of a potential field line of sight extrapolation. The figure shows some open loops ejecting from the center of the region followed by small closed loops along the outer edge of the extrapolated region, indicating the presence of a magnetic re-connection, or interchange re-connection, based event.

close outside of the region, in a sea of small closed loops. The proximity of open fields to closed loops suggests the occurrence of interchange reconnection as the mechanism for energy release which leads to the observed multifractal intensity signals in this case. In the QS among the network cases (41 total in Clusters 0 and 2) 59 % are (persistent, multifractal) and 41 % (anti-persistent, not multifractal). If the multifractality is associated with interchange reconnection between open and closed fields, these numbers are consistent with a lower density of open fields in the QS network and compared to the CH.

Among the non-network cases the classification into Clusters 1 and 3 was more approximate. Taking in consideration this caveat it is still reasonable to conclude that about for both the CH and QS regions about half of the cases are (persistent, multifractal) and the other half (anti-persistent, not multifractal). In these cases the underlying mechanisms could be reconnection among closed loops of different lengths, with a very small subset corresponding leading intermittent intensity emission.

For the region in between the boundaries the majority (71 %) of the cases in the network regions (35 total cases in Clusters 0 and 2) are (persistent, multifractal). This is precisely intermediate between the CH and QS results.



## 6. Conclusions and General Outlook

This project has used MF-DFA to study the scaling properties of intensity EUV 193 Å fluctuations in a CH and adjacent QS region, taking into consideration two possible definitions for the CH boundary. The results indicate that the CH and in between regions tend to have higher percentages of stationary persistent signals, as was shown by Cadavid et. al. (2019) (26), while the QS has a higher density of non-stationary anti-persistent signals compatible with an a possible underlying turbulent process. The CH, QS, and in-between boundary regions all present cases of monofractality, multifractality and noisy multifractality as classified in the literature for simulated data. The inclusion of the flux imbalance ratio allowed the classification of results into 4 clusters in the three-dimensional parameter space by using the k-means clustering algorithm. This led to the association of particular characteristics to each of the clusters which in turn facilitated the interpretation of the 190 results. The main results found are: (1) The intensity signals in the CH network regions are primarily characterized by (persistent, multifractal) properties; (2) The QS and the region between the boundaries in the network regions present both (persistent, multifractal) and (anti-persistent, not multifractal) cases with an inclination towards the first class; (3) away from the network the three physical regions present comparable percentages of cases in the (persistent, multifractal) and (anti-persistent, not multifractal) groups.

Since the region between the boundaries tends to have statistics slightly closer to those of the CH, it suggests that the CHIMERA method based on the thresholds of three EUV wavebands, and possibly with the information from the magnetic topology, may lead to a more accurate definition of the CH boundary.

The results can be further improved if the association of the physical characteristics with the clusters is done by defining more accurate boundaries between the regions instead of the rigid thresholds used for the three parameters.

It has been suggested that the network processes leading to persistent multifractality in the CH could result from interchange reconnection between open and closed magnetic field lines. It is noted that since this region has a low density of long loops as compared to the QS (Wiegelman

& Solanki, (2004) (55)), the majority of the interchange reconnection events may be occurring within shorter loops, and only a fraction would correspond to the mechanism described by Zank et. al. (2020) (6) which leads to the switchbacks in the solar wind. Away from the network perhaps the reconnection between closed loops could be associated with the anti-persistent, not multifractal signals. Another possibility is that these signals could be related to the "memory-less" turbulence described by Dudok de Wit et. al. (2020) (22). A natural next step would be to perform a systematic classification of potential field extrapolations for the various cases to get a full view of the magnetic topological context even if it is approximate.

# Bibliography

1. D. B. Jess *et al.*, **871**, 133, arXiv: 1812.06978 (astro-ph.SR) (Feb. 2019).
2. S. R. Cranmer, *Living Reviews in Solar Physics* **6**, 3, arXiv: 0909.2847 (astro-ph.SR) (Sept. 2009).
3. A. S. Krieger, A. F. Timothy, E. C. Roelof, **29**, 505–525 (Apr. 1973).
4. L. Abbo *et al.*, **201**, 55–108 (Nov. 2016).
5. S. R. Cranmer, S. E. Gibson, P. Riley, **212**, 1345–1384, arXiv: 1708.07169 (astro-ph.SR) (Nov. 2017).
6. G. P. Zank, M. Nakanotani, L. -Z. Zhao, L. Adhikari, J. Kasper, **903**, 1 (Nov. 2020).
7. T. H. Zurbuchen, L. A. Fisk, G. Gloeckler, R. von Steiger, **29**, 1352 (May 2002).
8. S. K. Antiochos, Z. Mikić, V. S. Titov, R. Lionello, J. A. Linker, **731**, 112, arXiv: 1102.3704 (astro-ph.SR) (Apr. 2011).
9. A. K. Higginson, S. K. Antiochos, C. R. DeVore, P. F. Wyper, T. H. Zurbuchen, **837**, 113, arXiv: 1611.04968 (astro-ph.SR) (Mar. 2017).
10. C. -Tu *et al.*, presented at the Solar Wind 11/SOHO 16, Connecting Sun and Heliosphere, ed. by B. Fleck, T. H. Zurbuchen, H. Lacoste, vol. 592, p. 131.
11. S. W. McIntosh *et al.*, **654**, 650–664, arXiv: astro-ph/0609503 (astro-ph) (Jan. 2007).
12. H. Tian, E. Marsch, C. Tu, W. Curdt, J. He, **54**, 13–30 (Jan. 2010).
13. J. Sheeley N. R., A. G. Nash, Y. -Wang, **319**, 481 (Aug. 1987).
14. M. S. Madjarska, T. Wiegmann, **503**, 991–997, arXiv: 0906.2556 (astro-ph.SR) (Sept. 2009).
15. S. Yang, J. Zhang, T. Li, Y. Liu, **732**, L7, arXiv: 1103.3751 (astro-ph.SR) (May 2011).
16. H. Tian, S. W. McIntosh, S. R. Habbal, J. He, **736**, 130, arXiv: 1105.3119 (astro-ph.SR) (Aug. 2011).
17. S. Subramanian, M. S. Madjarska, J. G. Doyle, **516**, A50, arXiv: 1002.1675 (astro-ph.SR) (June 2010).
18. E. Pariat, K. Dalmasse, C. R. DeVore, S. K. Antiochos, J. T. Karpen, **596**, A36, arXiv: 1609.08825 (astro-ph.SR) (Nov. 2016).
19. C. J. Schrijver, A. M. Title, A. A. van Ballegoijen, H. J. Hagenaar, R. A. Shine, **487**, 424–436 (Sept. 1997).
20. N. J. Fox *et al.*, **204**, 7–48 (Dec. 2016).
21. S. D. Bale *et al.*, **576**, 237–242 (Dec. 2019).
22. T. Dudok de Wit *et al.*, **246**, 39, arXiv: 1912.02856 (astro-ph.SR) (Feb. 2020).
23. S. Wedemeyer-Böhm, F. Wöger, presented at the Waves & Oscillations in the Solar Atmosphere: Heating and Magneto-Seismology, ed. by R. Erdélyi, C. A. Mendoza-Briceno, vol. 247, pp. 66–73, arXiv: 0710.4776 (astro-ph).
24. M. A. Reiss *et al.*, **913**, 28, arXiv: 2103.14403 (astro-ph.SR) (May 2021).
25. J. A. Klimchuk, presented at the AAS/AGU Triennial Earth-Sun Summit, 203.08, p. 203.08.
26. A. C. Cadavid, M. P. Miralles, K. Romich, **886**, 143, arXiv: 1910.09541 (astro-ph.SR) (Dec. 2019).
27. C.-K. Peng *et al.*, *Phys. Rev. E* **49**, 1685–1689, (<https://link.aps.org/doi/10.1103/PhysRevE.49.1685>) (2 Feb. 1994).
28. Z. Chen, P. C. Ivanov, K. Hu, H. E. Stanley, **65**, 041107, arXiv: physics/0111103 (physics.data-an) (Apr. 2002).
29. K. Hu, P. C. Ivanov, Z. Chen, P. Carpena, H. Eugene Stanley, *Phys. Rev. E* **64**, 011114, (<https://link.aps.org/doi/10.1103/PhysRevE.64.011114>) (1 June 2001).
30. J. W. Kantelhardt *et al.*, *Physica A Statistical Mechanics and its Applications* **316**, 87–114, arXiv: physics/0202070 (physics.data-an) (Dec. 2002).

31. Auchère, F., Bocchialini, K., Solomon, J., Tison, E., *A&A* **563**, A8, (<https://doi.org/10.1051/0004-6361/201322572>) (2014).
32. Gupta, G. R., *A&A* **568**, A96, (<https://doi.org/10.1051/0004-6361/201323200>) (2014).
33. A. C. Cadavid, J. K. Lawrence, D. J. Christian, D. B. Jess, G. Nigro, **795**, 48, arXiv: 1404.7824 (astro-ph.SR) (Nov. 2014).
34. J. Ireland, R. T. J. McAteer, A. R. Inglis, **798**, 1, arXiv: 1410.2171 (astro-ph.SR) (Jan. 2015).
35. K. P. Reardon, F. Lepreti, V. Carbone, A. Vecchio, *The Astrophysical Journal* **683**, L207–L210, (<https://doi.org/10.1086%2F591790>) (Aug. 2008).
36. J. K. Lawrence, A. C. Cadavid, D. J. Christian, D. B. Jess, M. Mathioudakis, **743**, L24, arXiv: 1111.4253 (astro-ph.SR) (Dec. 2011).
37. D. B. Jess *et al.*, **842**, 59, arXiv: 1705.06282 (astro-ph.SR) (June 2017).
38. J. Feder, in *Fractals* (Springer US, Boston, MA, 1988), pp. 66–103, ISBN: 978-1-4899-2124-6, ([https://doi.org/10.1007/978-1-4899-2124-6\\_6](https://doi.org/10.1007/978-1-4899-2124-6_6)).
39. R. Hardstone *et al.*, *Frontiers in physiology* **3**, 450 (Nov. 2012).
40. J. Beran, presented at the.
41. M. Gilmore, C. X. Yu, T. L. Rhodes, W. A. Peebles, *Physics of Plasmas* **9**, 1312–1317 (Apr. 2002).
42. B. B. Mandelbrot, J. W. V. Ness, *SIAM Review* **10**, 422–437, ISSN: 00361445, (2022; <http://www.jstor.org/stable/2027184>) (1968).
43. K. Ivanova, M. Ausloos, E. E. Clothiaux, T. P. Ackerman, *Europhysics Letters (EPL)* **52**, 40–46, (<https://doi.org/10.1209/epl/i2000-00401-5>) (Oct. 2000).
44. B. Malamud, D. Turcotte, *Natural Hazards* **20**, 93–116 (Nov. 1999).
45. J. W. Kantelhardt, R. Berkovits, S. Havlin, A. Bunde, *Physica A: Statistical Mechanics and its Applications* **266**, 461–464, ISSN: 0378-4371, (<https://www.sciencedirect.com/science/article/pii/S0378437198006311>) (1999).
46. T. D. de Wit *et al.*, *The Astrophysical Journal Supplement Series* **246**, 39, (<https://doi.org/10.3847/1538-4365/ab5853>) (Feb. 2020).
47. A. Davis, A. Marshak, W. Wiscombe, R. Cahalan, **99**, 8055–8072 (Apr. 1994).
48. C. Heneghan, G. McDarby, *Phys. Rev. E* **62**, 6103–6110, (<https://link.aps.org/doi/10.1103/PhysRevE.62.6103>) (5 Nov. 2000).
49. C. -. Tu, E. Marsch, **171**, 363–391 (Apr. 1997).
50. E. Ihlen, *Frontiers in Physiology* **3**, ISSN: 1664-042X, (<https://www.frontiersin.org/article/10.3389/fphys.2012.00141>) (2012).
51. M. Sadegh Movahed, E. Hermanis, *Physica A Statistical Mechanics and its Applications* **387**, 915–932, arXiv: physics/0608056 (physics.data-an) (Feb. 2008).
52. D. Grech, G. Pamula, *Physica A-statistical Mechanics and Its Applications* **392**, 5845–5864 (2013).
53. J. Ludescher, M. Bogachev, J. Kantelhardt, A. Y. Schumann, A. Bunde, *Physica A Statistical and Theoretical Physics* **390**, 2480 (July 2011).
54. J. Feder, P. Bak, *Physics Today* **42**, 90 (Sept. 1989).
55. T. Wiegmann, S. K. Solanki, *Solar Physics* **225**, 227–247, (<https://doi.org/10.1007%2Fs11207-004-3747-2>) (Dec. 2004).
56. C. E. Alissandrakis, **100**, 197–200 (July 1981).
57. S. Lloyd, *IEEE Transactions on Information Theory* **28**, 129–137 (1982).
58. E. W. Forgy, *Biometrics* **21**, 768–769 (1965).
59. R. L. Thorndike, *Psychometrika*, 267–276 (1953).

60. T. M. Garton, P. T. Gallagher, S. A. Murray, *Journal of Space Weather and Space Climate* **8**, A02, arXiv: 1711.11476 (astro-ph.SR) (Jan. 2018).
61. J. R. Lemen *et al.*, *Solar Physics* **275**, 17–40 (Jan. 2012).
62. W. D. Pesnell, B. J. Thompson, P. C. Chamberlin, **275**, 3–15 (Jan. 2012).
63. J. Schou *et al.*, **275**, 229–259 (Jan. 2012).
64. E. Samara *et al.*, *Astronomy & Astrophysics* **662**, A68, (<https://doi.org/10.1051%2F0004-6361%2F202142793>) (June 2022).
65. M. A. Reiss *et al.*, *The Astrophysical Journal* **913**, 28, (<https://doi.org/10.3847%2F1538-4357%2F2021042793>) (May 2021).
66. L. Krista, P. Gallagher, D. Bloomfield, *The Astrophysical Journal Letters* **731** (Mar. 2011).
67. T. M. Garton, S. A. Murray, P. T. Gallagher, *The Astrophysical Journal* **869**, L12, (<https://doi.org/10.3847%2F2041-8213%2Faaf39a>) (Dec. 2018).